

Intrinsic Image Fusion for Multi-View 3D Material Reconstruction

Peter Kocsis Lukas Höllein Matthias Nießner
Technical University of Munich

peter-kocsis.github.io/IntrinsicImageFusion/

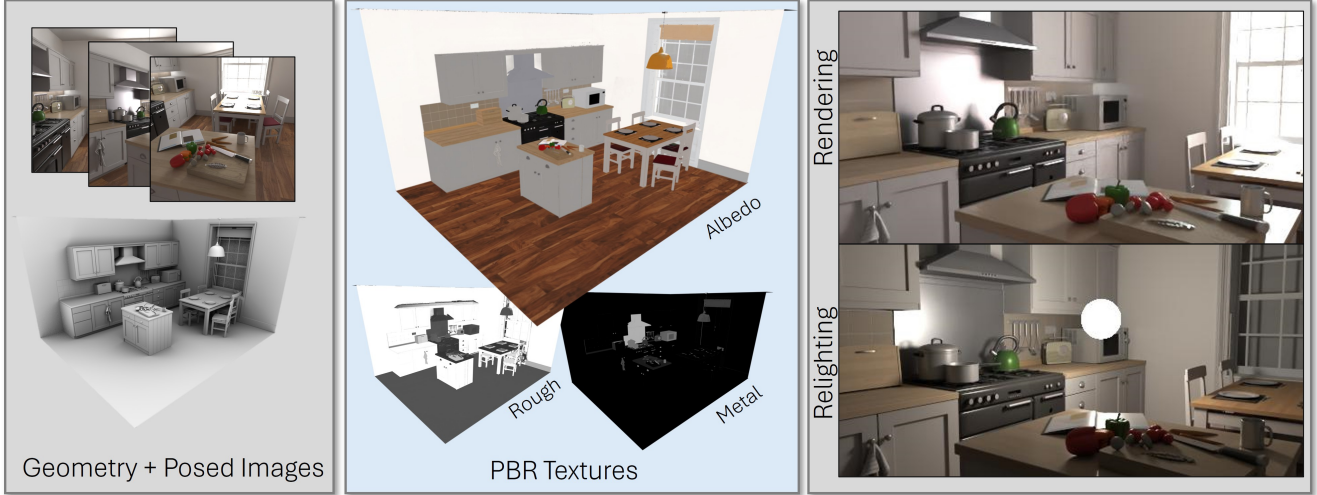


Figure 1. **Intrinsic Image Fusion (IIF)**. Our method reconstructs room-scale 3D physically based rendering (PBR) materials. Given multi-view images with reconstructed geometry, we obtain high-quality PBR textures by distilling 2D decomposition priors into a 3D-consistent space via inverse path-tracing. This enables downstream applications for content creation, suitable for rendering and relighting.

Abstract

We introduce *Intrinsic Image Fusion*, a method that reconstructs high-quality physically based materials from multi-view images. Material reconstruction is highly under-constrained and typically relies on analysis-by-synthesis, which requires expensive and noisy path tracing. To better constrain the optimization, we incorporate single-view priors into the reconstruction process. We leverage a diffusion-based material estimator that produces multiple, but often inconsistent, candidate decompositions per view. To reduce the inconsistency, we fit an explicit low-dimensional parametric function to the predictions. We then propose a robust optimization framework using soft per-view prediction selection together with confidence-based soft multi-view inlier set to fuse the most consistent predictions of the most confident views into a consistent parametric material space. Finally, we use inverse path tracing to optimize for the low-dimensional parameters. Our results outperform state-of-the-art methods in material disentanglement on both synthetic and real scenes, producing sharp and clean reconstructions suitable for high-quality relighting.

1. Introduction

Accurately decomposing indoor scenes into physically based rendering (PBR) components—such as albedo, roughness, metallic properties, and illumination—is a core task in computer graphics and vision. High-quality PBR decomposition enables a wide range of applications, including relighting, material editing, and virtual object insertion. Despite its importance, recovering these properties at room scale remains challenging.

Many inverse rendering approaches rely on path tracing to simulate the light transport in complex 3D scenes [1, 18, 25], but realistic renderings are computationally expensive and inherently noisy. This noise propagates into the optimization process, making it difficult to recover stable and accurate material estimates. In addition, appearance decomposition is fundamentally ambiguous: diffuse, specular, and lighting components are tightly coupled, particularly in complex indoor scenes with diverse geometries and light sources.

On the other hand, single image material estimators [12, 30] have seen unprecedented improvements in the re-

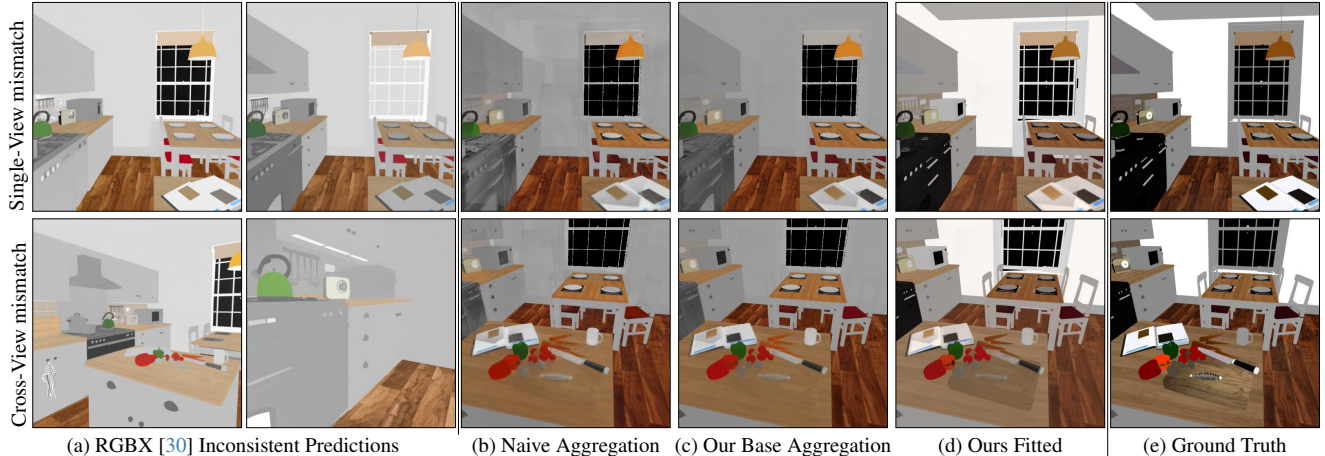


Figure 2. **Parametric PBR Aggregation.** (a) RGBX [30] predicts PBR maps from 2D images, but they are inconsistent within the same view (top) or across views (bottom). (b) Naively using them to texture an entire 3D scene results in visible continuity artifacts and blurred-out details. (c) We propose a parametric aggregation, that distills the rich prior of 2D models into 3D-consistent and sharp PBR textures. (d) Using inverse path tracing we further optimize for the free parameters of our textures to find a physically grounded decomposition.

cent years. Utilizing these 2D image priors of generative models have brought strong generalization capabilities, which enables high-quality material predictions solely from a single image. These models act probabilistically and are thus able to sample possible solutions of the ambiguous problem of appearance decomposition. Despite their high-quality results, patterns and relative reflectances are still inconsistently predicted across views, which is inherited from the probabilistic formulation. In contrast, explicit re-rendering from only a single image is still challenging due to the unobserved regions in complex 3D scenes.

To this end, we introduce Intrinsic Image Fusion, a method that embeds single-view decomposition models into an inverse rendering optimization scheme. This allows us to distill high-quality PBR textures for entire 3D scenes from strong 2D image priors. First, we use RGBX [30], a diffusion-based material estimator, to generate multiple candidate materials for each observed view of the 3D scene. From these candidates, we construct an explicit parametric distribution that captures the space of plausible materials. Specifically, we express the texture of each object as the combination of a linear basis function and an ambiguity-invariant base pattern. Furthermore, we model the variance of complex patterns by fitting a Laplacian distribution to multiple candidate predictions of the same object. Next, we aggregate these single-view distributions into a 3D-consistent texture through our novel parametric distribution matching. Finally, we use inverse rendering to optimize only for the remaining per-object parameters. Our hybrid approach yields sharp and consistent material estimates thanks to the pretrained predictions, while still being re-renderable thanks to the inverse path tracing. In summary, our main contributions are:

- We model the solution space of plausible materials using an explicit parametric distribution, drastically reducing the number of free parameters and thereby limiting the impact of rendering noise of inverse path tracing.
- We aggregate single-view material predictions into a consistent 3D parametric distributional texture using consistent distribution matching, which enables us to utilize the most consistent predictions, instead of averaging them.

2. Related Work

Inverse Rendering. The goal of inverse rendering is to reconstruct a virtual renderable representation of a 3D scene, usually from multi-view images. Traditional methods formulate an optimization problem using analysis-by-synthesis. The key challenge is how to efficiently synthesize the image in this process, because light transport estimation is generally very costly. Recent methods have shown really impressive results using inverse path tracing and using brilliant engineering solutions to make this expensive optimization tractable by optimizing hierarchically [1, 9, 20, 27, 29, 31, 34], alternating between light transport estimation and reflectance evaluation [25], introducing neural components [21]. The recent work of IRIS [18] even managed to extend to LDR inputs and has introduced a proxy material using per-object aggregation of a single-view material estimator [35]. However, rendering noise still poses a challenge for these methods and baked-in lighting, specular effects and geometric shading details are often noticeable in the diffuse materials. Our goal is to further reduce this noise by aggregating single-view predictions in a consistent manner and reduce the number of optimizable parameters.

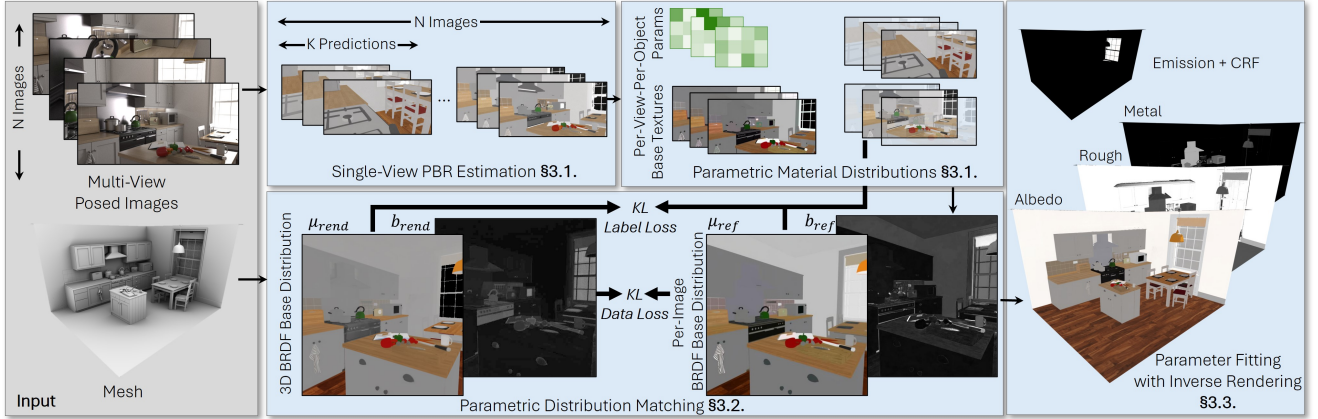


Figure 3. **Method Overview.** IIF takes multi-view posed input images and their reconstructed geometry as input. First, we estimate the materials for all the views using a monocular probabilistic estimator (§ 3.1). We define an explicit parametric distribution over the predictions consisting of a base texture together with a set of per-object parameters and aggregate the bases into a consistent 3D texture (§ 3.2). Then, we optimize for the free per-object parameters using inverse path tracing to get physically grounded albedo, rough and metal maps together with an emission texture and camera response function (CRF) suitable for complete rerendering.

Intrinsic Image Decomposition. Predicting material and lighting information only from a single image has a long-standing history. Early approaches focus on separating the reflectance from shading [8, 13, 24] using various heuristics, such as sparsity in reflectance properties [6, 7, 23, 32], or smoothness [2]. Later, deep-learning methods [15, 16, 35] train decomposition networks on synthetic datasets, such as [14, 17, 33]. Recently, [12, 30] formulate the ambiguous decomposition problem probabilistically using a diffusion model, thereby sampling from the solution space. Furthermore, utilizing the strong image prior of pretrained models enables unprecedented generalization to complex scenes and lighting conditions. Although these methods are able to produce impressive and sharp materials, their predictions are not necessarily physically correct and often prone to hallucination artifacts. Our method combines these model predictions with a rendering-based optimization to ensure physically correct and consistent textures for room-scale scenes.

3. Method

Our method optimizes a full PBR representation of a 3D scene: albedo, roughness, and metallic textures, together with an emission map and camera response function (CRF). Given a set of posed image observations and the corresponding 3D scene reconstruction as input, we turn this RGB-space representation into PBR-space. We combine single-view material priors [30] with inverse rendering to produce high-quality, disentangled material and lighting estimates. Concretely, we first define a parametric distribution of the single-view predictions (§ 3.1) and then aggregate them into a consistent 3D PBR representation (§ 3.2). Finally, we optimize for the free parameters using factorized

inverse path tracing ([25]), while accounting for LDR inputs ([18]) (§ 3.3). We show our overall pipeline in Fig. 3

3.1. Parametric single-view material distributions

Estimating materials requires disentangling reflectance from illumination while remaining consistent with physically accurate light transport. However, directly optimizing these quantities is difficult: photo-realistic evaluation of the rendering equation is computationally expensive, typically resulting in Monte-Carlo noise. This leads to high-variance gradients and instabilities in the recovered materials.

To this end we propose to leverage the powerful priors of 2D decomposition methods like RGBX [30]. Since decomposing from RGB-space into PBR-space is an under-constrained problem, such 2D methods model a distribution of possible solutions. As a result of this ambiguity, these predictions are not necessarily consistent within a view or across views (Figure 2a), which limits their direct applicability to 3D material reconstruction (Figure 2b). Our core idea is to transform these predictions into a consistent parametric space and model their variance as a distribution. This allows us to distill the predicted 2D PBR maps into consistent 3D PBR textures (Figure 2c).

Parametric BRDF. For each image observation of the scene, we predict K reference decompositions of albedo, roughness, and metallic maps using RGBX [30]. Since these raw material predictions are lying in the ambiguity-variant solution space, naive aggregation yields inconsistent textures (Figure 2b). The main ambiguity between lighting and reflectance is the scale invariance: it is hard to tell, whether the observed RGB color is caused by the reflectance or by the lighting. For example, multiple albedo colors are plausible for the kettle in Figure 2a. Inspired

by the color calibration literature, we parametrize the solution space via learnable affine transformations, that capture these ambiguities. Specifically, for each object in each prediction, we define a parametric model:

$$\begin{aligned}\bar{\mathbf{a}}_{i,k} &= T_{i,k}^a [\mathbf{a}_{i,k}, 1], & T_{i,k}^a &\in \mathbb{R}^{3 \times 4}, \\ \bar{\mathbf{r}}_{i,k} &= T_{i,k}^r [\mathbf{r}_{i,k}, 1], & T_{i,k}^r &\in \mathbb{R}^{1 \times 2}, \\ \bar{\mathbf{m}}_{i,k} &= T_{i,k}^m [\mathbf{m}_{i,k}, 1], & T_{i,k}^m &\in \mathbb{R}^{1 \times 2}\end{aligned}\quad (1)$$

where $\mathbf{a}_{i,k}$ are the albedo pixels of the i -th object in the k -th prediction of a given image observation, $T_{i,k}^a$ its corresponding affine transformation, and $\bar{\mathbf{a}}_{i,k}$ we call the albedo base texture. We similarly denote the quantities for roughness and metallic as \mathbf{r} and \mathbf{m} , respectively.

BRDF Distribution. Our parametric BRDF formulation can account for the per-object global inconsistencies across predictions, but it cannot solve inconsistencies in high-frequency patterns, such as on the countertop, which leads to oversmoothing, when aggregated in 3D (Figure 2b). Our goal is to find a distribution, whose mean is the most consistent prediction across all views. To this end, we model the solution space of a single view as a *per-image-per-object* Laplacian distribution.

First, we introduce learnable assignment logits for each object in each reference image, per material: $z_{i,k}^a \in \mathbb{R}$ for albedo and $z_{i,k}^r, z_{i,k}^m$ for roughness and metallic, respectively. We then compute the pixel-wise weighted mixture of reference predictions for each material property:

$$\alpha_{i,k}^a = \frac{\exp(z_{i,k}^a / \tau_{\text{logit}})}{\sum_{j=1}^K \exp(z_{i,k}^j / \tau_{\text{logit}})} \quad (2)$$

where τ_{logit} is a fixed temperature. We then define the location of the distribution as $\boldsymbol{\mu}_i^{\text{ref}} = [\bar{\mathbf{a}}_i, \bar{\mathbf{r}}_i, \bar{\mathbf{m}}_i]$, where $\bar{\mathbf{a}}_i = \sum_{k=1}^K \alpha_{i,k}^a \cdot \bar{\mathbf{a}}_{i,k}$, and $\bar{\mathbf{r}}_i$ and $\bar{\mathbf{m}}_i$ are obtained similarly.

To estimate the scale of the mixture, we compute the median deviation of the reference predictions from the mixture:

$$\mathbf{b}_i^{\text{ref}} = \text{median}_{k=1}^K \|\boldsymbol{\mu}_i^{\text{ref}} - [\bar{\mathbf{a}}_{i,k}, \bar{\mathbf{r}}_{i,k}, \bar{\mathbf{m}}_{i,k}]\| \quad (3)$$

We then define the Laplacian distribution of the reference predictions as $p_i^{\text{ref}} \sim \text{Laplace}(\boldsymbol{\mu}_i^{\text{ref}}, \mathbf{b}_i^{\text{ref}})$.

3.2. Distribution Matching Optimization

In order to obtain a 3D-consistent PBR texture of the whole scene, we utilize the *per-image-per-object* PBR distributions in a distribution matching optimization. In other words, the 3D PBR texture is similarly modeled as a Laplacian distribution and should be identical to the respective 2D distribution when rendered into images. This allows us to distill the rich 2D prior of models such as RGBX [30] into a consistent 3D PBR texture.

PBR Texture Model. During optimization, we randomly sample N pixels across all input images and retrieve the corresponding 3D coordinates $\mathbf{x}_n \in \mathbb{R}^3$ on the reconstructed

mesh. A BRDF network f_θ based on InstantNGP [19] predicts material properties and associated uncertainties at these 3D positions:

$$(\mathbf{a}_n, \boldsymbol{\sigma}_n^a), (\mathbf{r}_n, \boldsymbol{\sigma}_n^r), (\mathbf{m}_n, \boldsymbol{\sigma}_n^m) = f_\theta(\mathbf{x}_n) \quad (4)$$

We utilize these outputs to define the Laplacian distribution of the PBR texture as:

$$\begin{aligned}\boldsymbol{\mu}_n^{\text{pred}} &= [\mathbf{a}_n, \mathbf{r}_n, \mathbf{m}_n], \\ \mathbf{b}_n^{\text{pred}} &= [\boldsymbol{\sigma}_n^a, \boldsymbol{\sigma}_n^r, \boldsymbol{\sigma}_n^m], \\ p_n^{\text{pred}} &\sim \text{Laplace}(\boldsymbol{\mu}_n^{\text{pred}}, \mathbf{b}_n^{\text{pred}})\end{aligned}\quad (5)$$

Data Loss via Laplacian Distributions. We encourage the BRDF network predictions to match the reference mixture under the Laplacian distribution assumption, by computing the KL-divergence:

$$\mathcal{L}_{\text{data}} = \frac{1}{N} \sum_{n=1}^N D_{\text{KL}}(p_{i_n}^{\text{ref}} \| p_n^{\text{pred}}) \quad (6)$$

where i_n specifies which of the *per-image-per-object* 2D distributions to pick for the n -th sampled pixel.

Label Loss for Assignment Logits. In practice, we found that the assignment logits need to be regularized to reach stable results. We choose a simple L2 regularization between the rendered materials and each reference prediction:

$$\begin{aligned}\mathbf{E}_{n,k} &= \mathcal{L}_2(\boldsymbol{\mu}_n^{\text{pred}}, [\bar{\mathbf{a}}_{i_n,k}, \bar{\mathbf{r}}_{i_n,k}, \bar{\mathbf{m}}_{i_n,k}]) \\ q_{n,k} &= \frac{\exp(-\mathbf{E}_{n,k} / \tau_{\text{err}})}{\sum_{j=1}^K \exp(-\mathbf{E}_{n,j} / \tau_{\text{err}})}\end{aligned}\quad (7)$$

The label loss is then defined as:

$$\mathcal{L}_{\text{label}} = -\frac{1}{N} \sum_{n=1}^N \sum_{k=1}^K q_{n,k} \log[\alpha_{i_n,k}^a, \alpha_{i_n,k}^r, \alpha_{i_n,k}^m] \quad (8)$$

Optimization. The total loss combines the BRDF data term, the label regularization, and an identity-regularizer for the affine transformations:

$$\mathcal{L}_{\text{total}} = w_{\text{data}} \mathcal{L}_{\text{data}} + w_{\text{label}} \mathcal{L}_{\text{label}} + w_{\text{reg}} \mathcal{L}_{\text{reg}}(T) \quad (9)$$

The optimization jointly updates the BRDF network parameters θ , the assignment logits z , and the affine transformations T to distill a consistent 3D material texture from uncertain multi-view 2D predictions.

3.3. Parameter Fitting with Inverse Rendering

After aggregating the parametrized single-view predictions, we obtain a 3D texture of base distributions. However, these distributions are ambiguity-invariant per object; that is, they are consistent across views for each object, but they represent independent samples from the solution space. To obtain a physically-grounded decomposition, we optimize for per-object PBR parameters T_o^a, T_o^r, T_o^m of every 3D object o , which we achieve with analysis-by-synthesis.

To optimize through photo-realistic rendering, we use path tracing to solve the rendering equation [10]:

$$L_o(x, \omega_o) = L_e(x, \omega_o) + \int_{\Omega} f_r(x, \omega_i, \omega_o) L_i(x, \omega_i) (\omega_i \cdot \mathbf{n}_x) d\omega_i \quad (10)$$

where \mathbf{n}_x is the surface normal at point x .

We model the surface reflectance using the Cook-Torrance microfacet model [5]:

$$\begin{aligned} f_r(\mathbf{x}, \omega_i, \omega_o) &= f_{\text{diff}}(\mathbf{x}) + f_{\text{spec}}(\mathbf{x}, \omega_i, \omega_o) \\ f_{\text{diff}}(x) &= \frac{\mathbf{k}_d(x)}{\pi} \\ f_{\text{spec}}(\mathbf{x}, \omega_i, \omega_o) &= \frac{D(\mathbf{h}) F(\omega_i, \mathbf{h}, \mathbf{k}_s) G(\omega_i, \omega_o, \mathbf{h})}{4(\mathbf{n}_x \cdot \omega_i)(\mathbf{n}_x \cdot \omega_o)} \end{aligned} \quad (11)$$

where $\mathbf{k}_d(\mathbf{x}) = (1 - m(\mathbf{x}))\mathbf{a}(\mathbf{x})$, $\mathbf{k}_s(\mathbf{x}) = 0.04 \cdot (1 - m(\mathbf{x})) + \mathbf{a}(\mathbf{x})m(\mathbf{x})$, h is the half-angle, $D(h)$ is the microfacet normal distribution function, $F(\omega_i, h)$ is the Fresnel term, $G(\omega_i, \omega_o, h)$ is the geometric visibility term, $\mathbf{a}(x)$ is the albedo, $m(x)$ is the metallic at x , and \mathbf{n}_x is the surface normal. The roughness $\mathbf{r}(x)$ and metallic $\mathbf{m}(x)$ textures modulate the specular lobe and Fresnel behavior according to standard PBR conventions [5].

Path tracing approximates the rendering equation with Monte-Carlo sampling of the rendering integral, usually resulting in noisy estimates. This noise is then backpropagated into the parameters, often causing backed-in shading effects. Our method regularizes this optimization by drastically reducing the total number of trainable parameters. Instead of optimizing for the full BRDF texture, we only need to find the per-object transformations. To further reduce the variance, we follow [25] and do an alternating optimization.

1. Lighting Optimization. The scene illumination is represented as per-triangle uniform emission $\mathbf{E} = \{E_t\}_{t \in \mathcal{T}}$, where \mathcal{T} is the set of emissive triangles. We pre-filter triangles that are constantly oversaturated and optimize the remaining ones via inverse path tracing while keeping the BRDF f_{θ} fixed:

$$\mathcal{L}_{\text{light}} = \sum_{i,p} \|\hat{L}_o(\mathbf{x}, \omega_i; \mathbf{f}_{\theta}, \mathbf{E}) - \mathbf{I}_i(p)\|_2, \quad (12)$$

where \mathbf{I}_i is the radiance of view i , pixel p with position x . A volumetric diffuse radiance cache is used to approximate multi-bounce lighting L_i after the final bounce, and low-intensity triangles are pruned after several iterations to accelerate convergence.

2. Light Transport Caching. Second, we cache the light transport. We render diffuse and specular shading maps, containing per-pixel pre-integrated lighting information [25]. Since this step does not involve any optimization, we can allow an estimation with higher sample count.

3. BRDF Parameter Fitting. Finally, we optimize for the per-object parameters T_o^a, T_o^r, T_o^m of our BRDF texture. We render the scene using the equation from FIPT. To account

Method	Albedo			Rough		Metal	Emit
	PSNR \uparrow	SSIM \uparrow	LPIPS \downarrow	L2 \downarrow	L2 \downarrow		
NeILF++ [31]	13.18	0.733	0.375	0.103	0.047	N/A	
FIPT [25]	10.63	0.661	0.403	0.110	0.006	2.208	
IRIS [18]	15.86	0.735	0.307	0.056	0.040	2.046	
IIF (Ours)	20.72	0.846	0.201	0.028	0.007	0.384	

Table 1. **Baseline comparisons.** We show quantitative results averaged over all the views of our four synthetic scenes Section 4. Our parametric formulation gives more constraints to inverse path tracing, yielding consistent and sharp predictions, outperforming the baselines by a high margin.

for LDR inputs, we jointly optimize for CRF parameters, following [18].

4. Experiments

Implementation details. We use $K=16$ predictions per view and aggregate them using Adam [11] optimizer (bs=65536, lr= $1e-2$, decayed by 0.5 every 2 epochs) with weights $w_{\text{data}}=w_{\text{label}}=1, w_{\text{reg}}=1e+2$. We anneal the temperatures $\tau_{\text{err}}=\tau_{\text{logit}}=1$ every 100 iterations by 0.85. We run the distribution matching optimization for 10 epochs, which takes approximately 5 minutes. Our parameter fitting follows the implementation in FIPT [25] using Mitsuba 3[9] and converges in approximately 55 minutes on a single A6000 GPU.

Test Scenes. We provide evaluations on the synthetic scenes from [3]. We transform the scenes into Blender [4] and unify all the BRDFs to make sure that the renderings follow our BRDF. Finally, we render all the modalities together with instance segmentations from multiple viewpoints at 512x512 resolution.

For our real evaluations, we use ScanNet++ [28] (2a1b555966, 651dc6b4f1). As geometry, we use the laser scan mesh. Although the laser scan provides high-quality surface information, it contains holes and reflective surfaces, such as windows are not reconstructed. To account for this, we extend our lighting representation for these scenes with an environment map of resolution 16x32 wrapped around a scene. To obtain 3D consistent instance segmentation, we use MaskClustering [26] with SAM [22] predictions. We provide additional details on the data pre-processing in our supplemental.

4.1. Comparisons

We compare our method against the recent inverse rendering methods using inter-reflection constraints (Neilf++ [31]), inverse path tracing (FIPT [25]) and using pre-trained priors (IRIS [18]). For all baselines, we use their released implementations and retrain/optimize on our datasets for fair comparisons. For IRIS [18], we used our RGBX [30] predictions for their regularization to ensure consistency

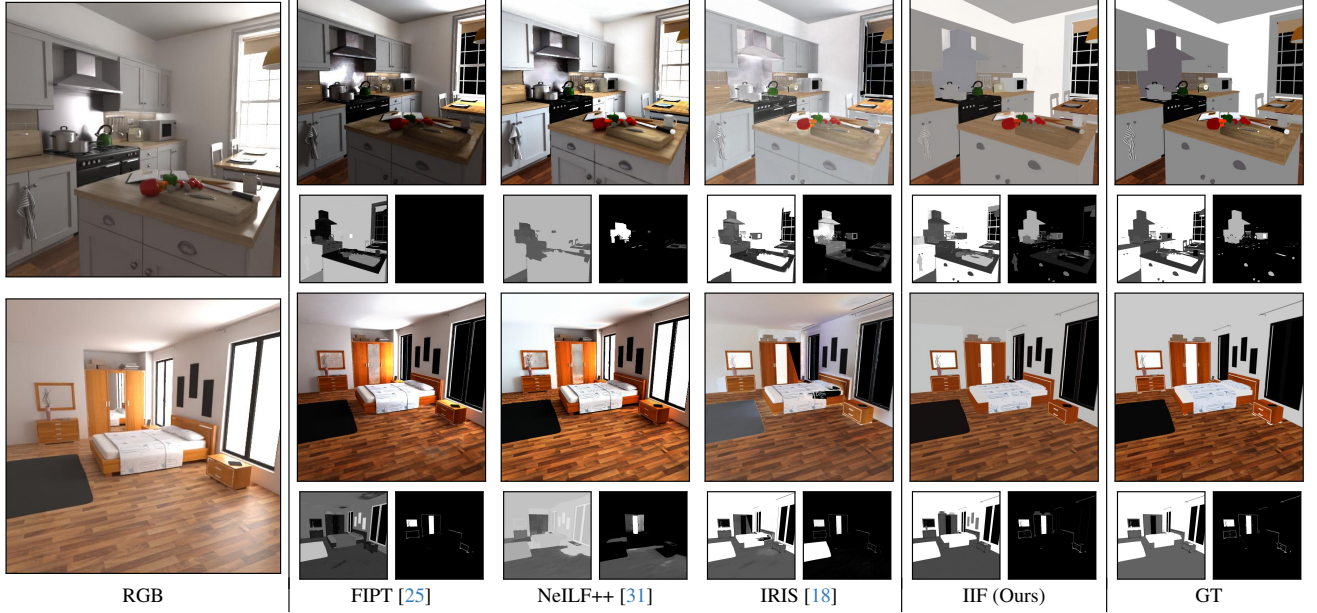


Figure 4. **Synthetic comparisons.** Previous inverse-rendering approaches often struggle to separate shading from reflectance due to the noise inherent in light-transport estimation, resulting in baked-in illumination and biased specular parameters [25, 31]. In contrast, our method restricts path-traced optimization to a low-dimensional set of per-object transformations, yielding a more constrained and stable objective. This leads to clean, sharp, and physically consistent material predictions.

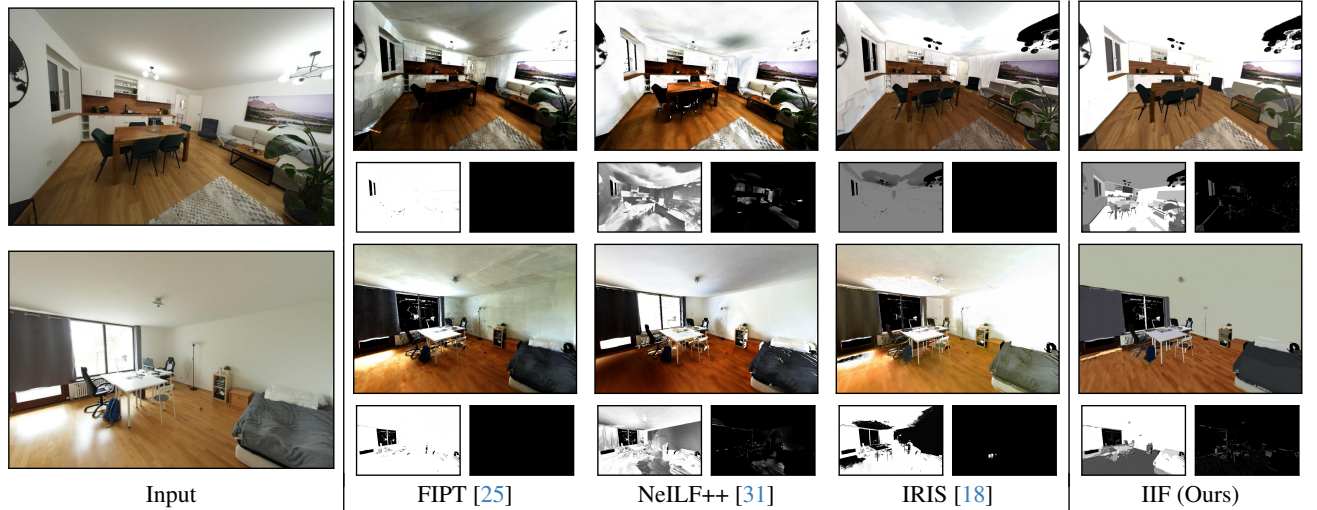


Figure 5. **Real-world comparisons.** Incomplete and noisy geometry poses a challenge for previous methods, yielding projected contour artifacts in the final textures (e.g., chair borders visible on the walls on the top). Our method uses a much more constrained objective able to maintain clean and consistent predictions. Please see the supplemental for animated flythroughs.

with our method. For the qualitative and quantitative evaluations, we ignore the BRDF parameters for the emitters, and the albedo for perfectly specular surfaces.

We provide qualitative comparisons on both synthetic (Figure 4) and real scenes (Figure 5). Due to the noisy estimation of light transport, earlier methods struggle with decoupling shading from reflectance, leading to strong baked-

in lighting and shifted specular parameters [25, 31]. IRIS [18] constrains the optimization by introducing pre-trained prior predictions as regularizer. However, they are still optimizing the whole texture via the noisy rendering loss, causing baked-in shading effects. In contrast, our method optimizes only for the low-dimensional per-object transformations with path-tracing, while fixing the BRDF network

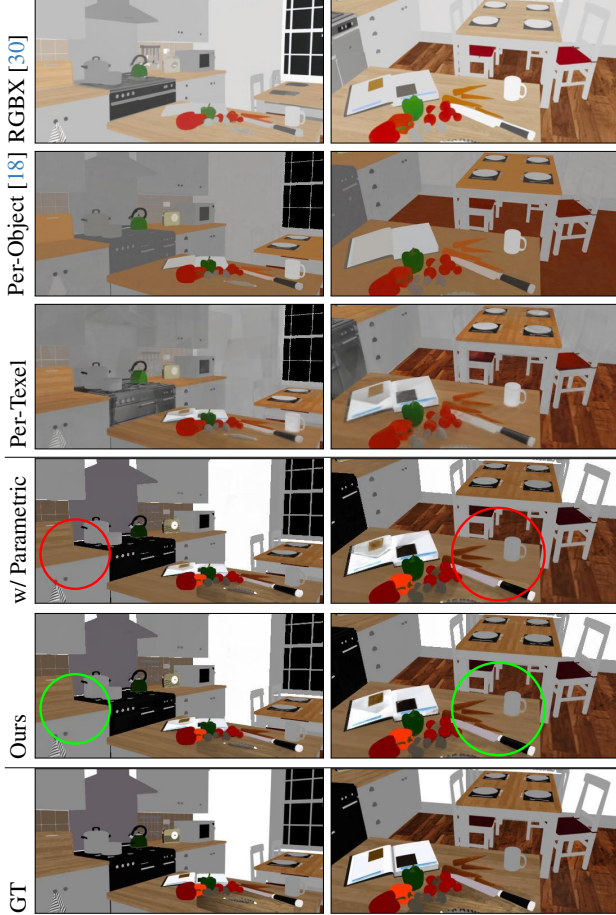


Figure 6. **Cross-view aggregation.** Single-view material estimation can yield detailed, but inconsistent predictions (Fig. 2), which are physically not well-grounded. IRIS [18] uses a per-object aggregation as a material proxy, causing loss of the patterns. Per-textel aggregation could maintain the patterns, but yields texture seams due to the inconsistencies. Our parametric modeling (§ 3.1) introduces an expressive, but low-dimensional space of possible consistent 3D aggregations. To avoid oversmoothing of local patterns, our distribution matching (§ 3.2) aims to use a single best prediction per view, giving more fine-grained details.

f_{θ} . This leads to clean/sharp materials, even on challenging real-world scenes (additional results in the supplemental).

We provide quantitative comparisons on the synthetic scenes. First, we render all PBR modalities for all views of the four synthetic datasets. Then, we report averaged comparisons against the respective ground-truth in Table 1. Our method outperforms previous approaches by a high margin and yields competitive results on the sparse metallic maps.

4.2. Ablations

Parametric model complexity. We study the importance of the parametric model in Fig. 7 by comparing our *per-image-per-object* model against a simpler *per-image* model

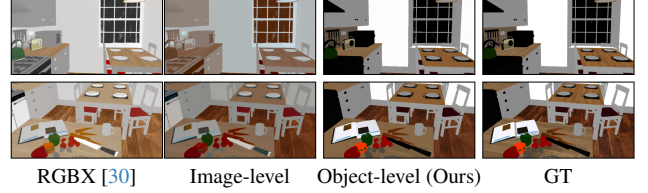


Figure 7. **Parametric Model.** We visualize the expressivity of different parametric model choices. Image-level fitting cannot correct erroneous relative reflectances between objects, while optimizing object segments independently provides significantly higher expressivity.

#Preds	Albedo			Rough	
	PSNR \uparrow	SSIM \uparrow	LPIPS \downarrow	L2 \downarrow	Metal L2 \downarrow
RGBX [30]	13.11	0.787	0.228	0.187	0.306
Per-Object Mean [18]	13.21	0.641	0.563	0.169	0.307
Per-Object Mean	13.43	0.753	0.42	0.170	0.308
w/ Parametric (§ 3.1)	29.53	0.909	0.176	8.16e-4	1.36e-4
Ours full (§ 3.2)	30.79	0.931	0.160	7.86e-4	1.34e-4

Table 2. **Effect of our aggregation.** We evaluate the expressivity of different aggregations of single-view RGBX [30] predictions. Per-object and per-textel aggregation improve consistency and PSNR but fail to preserve fine patterns (SSIM, LPIPS). Our parametric formulation can drastically improve the quality, while maintaining low parameter count. Our full method using distribution matching (§ 3.2) aims to use a single prediction per image to avoid oversmoothing, yielding improved quality.

that does not require object segmentations. While this simpler model also yields a stable optimization, it is not expressive enough and underfits (e.g., Fig. 7 shows an average color tone across objects). This hinders finding consistent 3D PBR textures in the subsequent optimization, leading to oversmoothed results. In contrast, our choice of *per-image-per-object* linear function captures detailed textures.

Cross-view aggregation. We ablate our design choices on the aggregation of the single-view predictions (Figure 6, Table 2). The single-view predictions of RGBX [30] provide a good prior over the patterns, but cannot be directly used for 3D texturing (Figure 2b). Per-object single color aggregation as in [1, 18] can make the predictions multi-view consistent, but removes a lot of details. Per-textel aggregation enables 3D consistent details, but suffers from texture seams caused by inconsistent predictions. We show that introducing our parametric texture model (Equation (1)) drastically improves the expressivity of the prior texture. Additionally, using our Laplace distribution matching optimization (§ 3.2) can further improve the quality by avoiding oversmoothing of local patterns.

Number of predictions. We quantify the effect of our Laplace distribution matching optimization (§ 3.2) by evaluating the aggregation quality using different number of



Figure 8. **Applications.** We show rerenderings of the scene and relighting by inserting emissive spheres into the scene. Our clean material decompositions enable high-quality renderings without baked-in lighting effects and correct specular highlights.

#Preds	Albedo			Rough		Metal	
	PSNR \uparrow	SSIM \uparrow	LPIPS \downarrow	L2 ($\times 1000$) \downarrow	L2 ($\times 1000$) \downarrow	L2 ($\times 1000$) \downarrow	L2 ($\times 1000$) \downarrow
1	29.62	0.908	0.177	0.817		0.134	
2	29.77	0.910	0.168	0.799		0.132	
4	30.37	0.926	0.160	0.795		0.134	
8	30.72	0.930	0.160	0.788		0.135	
(Ours) 16	30.79	0.931	0.160	0.786		0.134	

Table 3. **Effect of number of predictions.** The distilled 3D PBR textures improve with more 2D predictions without oversmoothing. This shows the advantage of our distribution matching (§ 3.2).

predictions (Table 3). Using more predictions improves the quality, showing that our aggregation does not oversmooth if having more predictions, but aims to find the most consistent one out of them. In other words, modelling the PBR distribution via many separate predictions is beneficial for finding a high-quality and 3D-consistent PBR texture.

4.3. Applications

By explicitly disentangling the PBR materials and lighting, our method enables high-quality relighting of room-scale 3D scenes (Figure 8). Our clean and sharp material textures do not contain any diffuse baked-in lighting patterns (e.g., smooth walls) and produce realistic specular reflections (e.g., bedroom mirror, around the kitchen oven). Please see the supplemental for animated relighting effects.

4.4. Limitations

While our method significantly improves material reconstruction, we rely on fixed geometry and inherit artifacts from the underlying mesh. Jointly optimizing for the geometry is possible and an interesting direction. Furthermore, sampling multiple possible material predictions is computationally costly. Incorporating the pre-trained prior directly into the optimization process could lead to a more compact approach. Finally, our method relies on the quality of pre-trained material estimators. Incorporating prediction uncertainties could be used to ignore incorrect predictions.

5. Conclusion

We have presented Intrinsic Image Fusion, a probabilistic inverse rendering framework for reconstructing high-quality PBR materials in room-scale indoor scenes. Our approach combines single-view generative priors with multi-view optimization, introducing a parametric material representation that reduces the impact of rendering noise while preserving fine details. By formulating the problem probabilistically, we explicitly account for uncertainty in both the priors and the path-traced gradients, enabling robust and consistent reconstructions. Our experiments demonstrate that Intrinsic Image Fusion outperforms state-of-the-art inverse rendering and intrinsic decomposition methods, delivering sharp, disentangled materials suitable for relighting, editing, and virtual object insertion. We believe Intrinsic Image Fusion provides a step toward practical, physically faithful scene decomposition.

Acknowledgements. This work was supported by Huawei as well as the ERC Starting Grant Scan2CAD (804724). We thank Angela Dai for the video voice-over and David Rozenberszki for the valuable discussions about the real-world instance segmentations.

References

- [1] Dejan Azinovic, Tzu-Mao Li, Anton Kaplanyan, and Matthias Nießner. Inverse path tracing for joint material and lighting estimation. In *IEEE Conference on Computer Vision and Pattern Recognition, CVPR 2019, Long Beach, CA, USA, June 16-20, 2019*, pages 2447–2456. Computer Vision Foundation / IEEE, 2019. 1, 2, 7
- [2] Sean Bell, Kavita Bala, and Noah Snavely. Intrinsic images in the wild. *ACM Trans. Graph.*, 33(4):159:1–159:12, 2014. 3
- [3] Benedikt Bitterli. Rendering resources, 2016. <https://benedikt-bitterli.me/resources/>. 5
- [4] Blender Online Community. *Blender - a 3D modelling and rendering package*. Blender Foundation, Stichting Blender Foundation, Amsterdam, 2018. 5
- [5] Robert L. Cook and Kenneth E. Torrance. A reflectance model for computer graphics. In *Proceedings of the 8th Annual Conference on Computer Graphics and Interactive Techniques, SIGGRAPH 1981, Dallas, Texas, USA, August 3-7, 1981*, pages 307–316. ACM, 1981. 5
- [6] Graham D. Finlayson, Mark S. Drew, and Cheng Lu. Intrinsic images by entropy minimization. In *Computer Vision - ECCV 2004, 8th European Conference on Computer Vision, Prague, Czech Republic, May 11-14, 2004. Proceedings, Part III*, pages 582–595. Springer, 2004. 3
- [7] Roger B. Grosse, Micah K. Johnson, Edward H. Adelson, and William T. Freeman. Ground truth dataset and baseline evaluations for intrinsic image algorithms. In *IEEE 12th International Conference on Computer Vision, ICCV 2009, Kyoto, Japan, September 27 - October 4, 2009*, pages 2335–2342. IEEE Computer Society, 2009. 3
- [8] Berthold KP Horn. Determining lightness from an image. *Computer graphics and image processing*, 3(4):277–299, 1974. 3
- [9] Wenzel Jakob, Sébastien Speierer, Nicolas Roussel, Merlin Nimier-David, Delio Vicini, Tizian Zeltner, Baptiste Nicolet, Miguel Crespo, Vincent Leroy, and Ziyi Zhang. Mitsuba 3 renderer, 2022. <https://mitsuba-renderer.org>. 2, 5
- [10] James T. Kajiya. The rendering equation. In *Proceedings of the 13th Annual Conference on Computer Graphics and Interactive Techniques, SIGGRAPH 1986, Dallas, Texas, USA, August 18-22, 1986*, pages 143–150. ACM, 1986. 4
- [11] Diederik P. Kingma and Jimmy Ba. Adam: A method for stochastic optimization. In *3rd International Conference on Learning Representations, ICLR 2015, San Diego, CA, USA, May 7-9, 2015, Conference Track Proceedings*, 2015. 5
- [12] Peter Kocsis, Vincent Sitzmann, and Matthias Nießner. Intrinsic image diffusion for indoor single-view material estimation. In *IEEE/CVF Conference on Computer Vision and Pattern Recognition, CVPR 2024, Seattle, WA, USA, June 16-22, 2024*, pages 5198–5208. IEEE, 2024. 1, 3
- [13] Edwin H Land and John J McCann. Lightness and retinex theory. *Josa*, 61(1):1–11, 1971. 3
- [14] Zhengqi Li and Noah Snavely. Cgintrinsics: Better intrinsic image decomposition through physically-based rendering. In *Computer Vision - ECCV 2018 - 15th European Conference, Munich, Germany, September 8-14, 2018, Proceedings, Part III*, pages 381–399. Springer, 2018. 3
- [15] Zhengqi Li and Noah Snavely. Learning intrinsic image decomposition from watching the world. In *2018 IEEE Conference on Computer Vision and Pattern Recognition, CVPR 2018, Salt Lake City, UT, USA, June 18-22, 2018*, pages 9039–9048. Computer Vision Foundation / IEEE Computer Society, 2018. 3
- [16] Zhengqin Li, Mohammad Shafiei, Ravi Ramamoorthi, Kalyan Sunkavalli, and Manmohan Chandraker. Inverse rendering for complex indoor scenes: Shape, spatially-varying lighting and SVBRDF from a single image. In *2020 IEEE/CVF Conference on Computer Vision and Pattern Recognition, CVPR 2020, Seattle, WA, USA, June 13-19, 2020*, pages 2472–2481. Computer Vision Foundation / IEEE, 2020. 3
- [17] Zhengqin Li, Ting-Wei Yu, Shen Sang, Sarah Wang, Meng Song, Yuhua Liu, Yu-Ying Yeh, Rui Zhu, Nitesh B. Gundavarapu, Jia Shi, Sai Bi, Hong-Xing Yu, Zexiang Xu, Kalyan Sunkavalli, Milos Hasan, Ravi Ramamoorthi, and Manmohan Chandraker. Openrooms: An open framework for photorealistic indoor scene datasets. In *IEEE Conference on Computer Vision and Pattern Recognition, CVPR 2021, virtual, June 19-25, 2021*, pages 7190–7199. Computer Vision Foundation / IEEE, 2021. 3
- [18] Chih-Hao Lin, Jia-Bin Huang, Zhengqin Li, Zhao Dong, Christian Richardt, Tuotuo Li, Michael Zollhöfer, Johannes Kopf, Shenlong Wang, and Changil Kim. IRIS: inverse rendering of indoor scenes from low dynamic range images. In *IEEE/CVF Conference on Computer Vision and Pattern Recognition, CVPR 2025, Nashville, TN, USA, June 11-15, 2025*, pages 465–474. Computer Vision Foundation / IEEE, 2025. 1, 2, 3, 5, 6, 7, 4
- [19] Thomas Müller, Alex Evans, Christoph Schied, and Alexander Keller. Instant neural graphics primitives with a multiresolution hash encoding. *ACM Trans. Graph.*, 41(4):102:1–102:15, 2022. 4, 1
- [20] Merlin Nimier-David, Zhao Dong, Wenzel Jakob, and Anton Kaplanyan. Material and lighting reconstruction for complex indoor scenes with texture-space differentiable rendering. In *32nd Eurographics Symposium on Rendering, EGSR 2021 - Digital Library Only Track, Saarbrücken, Germany, June 29 - July 2, 2021*, pages 73–84. Eurographics Association, 2021. 2
- [21] Julien Philip, Sébastien Morgethaller, Michaël Gharbi, and George Drettakis. Free-viewpoint indoor neural relighting from multi-view stereo. *ACM Transactions on Graphics (TOG)*, 40(5):1–18, 2021. 2
- [22] Nikhila Ravi, Valentin Gabeur, Yuan-Ting Hu, Ronghang Hu, Chaitanya Ryali, Tengyu Ma, Haitham Khedr, Roman Rädle, Chloé Rolland, Laura Gustafson, Eric Mintun, Junting Pan, Kalyan Vasudev Alwala, Nicolas Carion, Chao-Yuan Wu, Ross B. Girshick, Piotr Dollár, and Christoph

- Feichtenhofer. SAM 2: Segment anything in images and videos. In *The Thirteenth International Conference on Learning Representations, ICLR 2025, Singapore, April 24-28, 2025*. OpenReview.net, 2025. 5, 1
- [23] Li Shen, Ping Tan, and Stephen Lin. Intrinsic image decomposition with non-local texture cues. In *2008 IEEE Computer Society Conference on Computer Vision and Pattern Recognition (CVPR 2008)*, 24-26 June 2008, Anchorage, Alaska, USA. IEEE Computer Society, 2008. 3
- [24] Jiaye Wu, Sanjoy Chowdhury, Hariharmano Shanmugaraja, David Jacobs, and Soumyadip Sengupta. Measured albedo in the wild: Filling the gap in intrinsics evaluation. In *IEEE International Conference on Computational Photography, ICCP 2023, Madison, WI, USA, July 28-30, 2023*, pages 1–12. IEEE, 2023. 3
- [25] Liwen Wu, Rui Zhu, Mustafa B. Yaldiz, Yinhao Zhu, Hong Cai, Janarбек Matai, Fatih Porikli, Tzu-Mao Li, Manmohan Chandraker, and Ravi Ramamoorthi. Factorized inverse path tracing for efficient and accurate material-lighting estimation. In *IEEE/CVF International Conference on Computer Vision, ICCV 2023, Paris, France, October 1-6, 2023*, pages 3825–3835. IEEE, 2023. 1, 2, 3, 5, 6
- [26] Mi Yan, Jiazhao Zhang, Yan Zhu, and He Wang. Maskclustering: View consensus based mask graph clustering for open-vocabulary 3d instance segmentation. In *IEEE/CVF Conference on Computer Vision and Pattern Recognition, CVPR 2024, Seattle, WA, USA, June 16-22, 2024*, pages 28274–28284. IEEE, 2024. 5, 1
- [27] Yao Yao, Jingyang Zhang, Jingbo Liu, Yihang Qu, Tian Fang, David McKinnon, Yanghai Tsin, and Long Quan. Neilf: Neural incident light field for physically-based material estimation. In *Computer Vision - ECCV 2022 - 17th European Conference, Tel Aviv, Israel, October 23-27, 2022, Proceedings, Part XXXI*, pages 700–716. Springer, 2022. 2
- [28] Chandan Yeshwanth, Yueh-Cheng Liu, Matthias Nießner, and Angela Dai. Scannet++: A high-fidelity dataset of 3d indoor scenes. In *IEEE/CVF International Conference on Computer Vision, ICCV 2023, Paris, France, October 1-6, 2023*, pages 12–22. IEEE, 2023. 5, 1, 3
- [29] Bohan Yu, Siqi Yang, Xuanning Cui, Siyan Dong, Baoquan Chen, and Boxin Shi. MILO: multi-bounce inverse rendering for indoor scene with light-emitting objects. *IEEE Trans. Pattern Anal. Mach. Intell.*, 45(8):10129–10142, 2023. 2
- [30] Zheng Zeng, Valentin Deschaintre, Iliyan Georgiev, Yannick Hold-Geoffroy, Yiwei Hu, Fujun Luan, Ling-Qi Yan, and Milos Hasan. $\text{Rgb} \leftrightarrow \text{x}$: Image decomposition and synthesis using material- and lighting-aware diffusion models. In *ACM SIGGRAPH 2024 Conference Papers, SIGGRAPH 2024, Denver, CO, USA, 27 July 2024- 1 August 2024*, page 75. ACM, 2024. 1, 2, 3, 4, 5, 7
- [31] Jingyang Zhang, Yao Yao, Shiwei Li, Jingbo Liu, Tian Fang, David McKinnon, Yanghai Tsin, and Long Quan. Neilf++: Inter-reflectable light fields for geometry and material estimation. In *IEEE/CVF International Conference on Computer Vision, ICCV 2023, Paris, France, October 1-6, 2023*, pages 3578–3587. IEEE, 2023. 2, 5, 6, 3
- [32] Qing Zhang, Jin Zhou, Lei Zhu, Wei Sun, Chunxia Xiao, and Wei-Shi Zheng. Unsupervised intrinsic image decomposition using internal self-similarity cues. *IEEE Trans. Pattern Anal. Mach. Intell.*, 44(12):9669–9686, 2022. 3
- [33] Jingsen Zhu, Fujun Luan, Yuchi Huo, Zihao Lin, Zhihua Zhong, Dianbing Xi, Rui Wang, Hujun Bao, Jiaxiang Zheng, and Rui Tang. Learning-based inverse rendering of complex indoor scenes with differentiable monte carlo raytracing. In *SIGGRAPH Asia 2022 Conference Papers*. ACM, 2022. 3
- [34] Jingsen Zhu, Yuchi Huo, Qi Ye, Fujun Luan, Jifan Li, Dianbing Xi, Lisha Wang, Rui Tang, Wei Hua, Hujun Bao, and Rui Wang. I^2 -sdf: Intrinsic indoor scene reconstruction and editing via raytracing in neural sdf. In *IEEE/CVF Conference on Computer Vision and Pattern Recognition, CVPR 2023, Vancouver, BC, Canada, June 17-24, 2023*, pages 12489–12498. IEEE, 2023. 2
- [35] Rui Zhu, Zhengqin Li, Janarбек Matai, Fatih Porikli, and Manmohan Chandraker. Irisformer: Dense vision transformers for single-image inverse rendering in indoor scenes. In *IEEE/CVF Conference on Computer Vision and Pattern Recognition, CVPR 2022, New Orleans, LA, USA, June 18-24, 2022*, pages 2812–2821. IEEE, 2022. 2, 3

Intrinsic Image Fusion for Multi-View 3D Material Reconstruction

Supplementary Material

A. Additional Implementational Details

Number of parameters. Our parametric texture representations use a base texture and a set of per-object affine transformations. The base texture uses a neural hashgrid [19] with 32 levels, 2 features per level and 2^{19} hashmap size to store albedo, rough, metallic means and scales, which amounts to 28 M parameters. These base texture parameters are optimized only during the aggregation phase. During the inverse path tracing, we only need to optimize the per-object affine transformations, which amounts to $O \times 3 \times 4$, where O is the number of 3D objects, giving a total of 1092 parameters for the kitchen scene. Optimizing on such a low-dimensional manifold makes the inverse path tracing more constrained, making it more robust against the rendering noise.

Real data pre-processing. Our method relies on instance segmentation, which we obtain in a pre-processing step for the ScanNet++ [28] scenes. We use SAM2 [22] to estimate a per-image segmentation. To aggregate the segmentations, we use MaskClustering [26]. This way, we get a per-face instance id. Then, we rasterize the mesh into all the views and render the instance ids to get per-pixel instances. These images are only used for evaluating the baseline IRIS [18].

Real-world lighting representation. To account for missing geometry and emission coming from outside of the scene, we additionally define an environment map of resolution 16×32 . Similarly to the mesh emission, we filter the potentially emissive environment map pixels by thresholding their aggregated observed radiance values ($t = 0.85$).

Lighting optimization. Our lighting optimization follows FIPT [25] and has four steps. First, we initialize the emissive triangles by filtering the aggregated observed radiance with a threshold of $t = 0.99$. Second, we optimize for the emission values using frozen base material textures with inverse path tracing using 128 samples per pixel with a single bounce. We use SGD optimizer for 1 epoch and batch size 8192 rays with initial learning rate of $lr = 1e + 2$. After 1000 iterations, we prune all the emitters, which has an intensity lower than 5% of the overall maximum intensity. This stage takes 35 minutes using 20 GB of VRAM on the kitchen scene. Then, we cache the light transport into diffuse ($spp = 256$) and specular shading maps ($spp = 128$). This stage takes 5 minutes on the kitchen scene. Finally, we optimize for the BRDF and CRF parameters by re-rendering

with the cached shading maps. This stage takes 20 minutes using 11 GB of VRAM on the kitchen scene. Here, we use SGD optimizer for 3 epoch and batch size 32768 rays with initial learning rate of $lr = 1e + 1$ and decay after every epoch by a factor of 0.2. Following IRIS [18], we regularize the roughness and metallic channels to stay close to diffuse materials ($w_{rough} = 1e - 3$, $w_{metal} = 5e - 3$).

B. Additional Results

Our supplementary video provides comparisons and relightings with rendered trajectories. We provide additional results for all the synthetic scenes in Figure 9, for the real ScanNet++ (2a1b555966, 651dc6b4f1, a003a6585e) scenes in Figure 10. We compare also on the real scenes of FIPT [25] in Figure 11, which uses photo-metric stereo for the mesh reconstruction. Additionally, we provide additional relighting results on synthetic and ScanNet++ [28] scenes in Figure 12. Finally, we provide additional ablation results on our cross-view aggregation strategies in Figure 13.

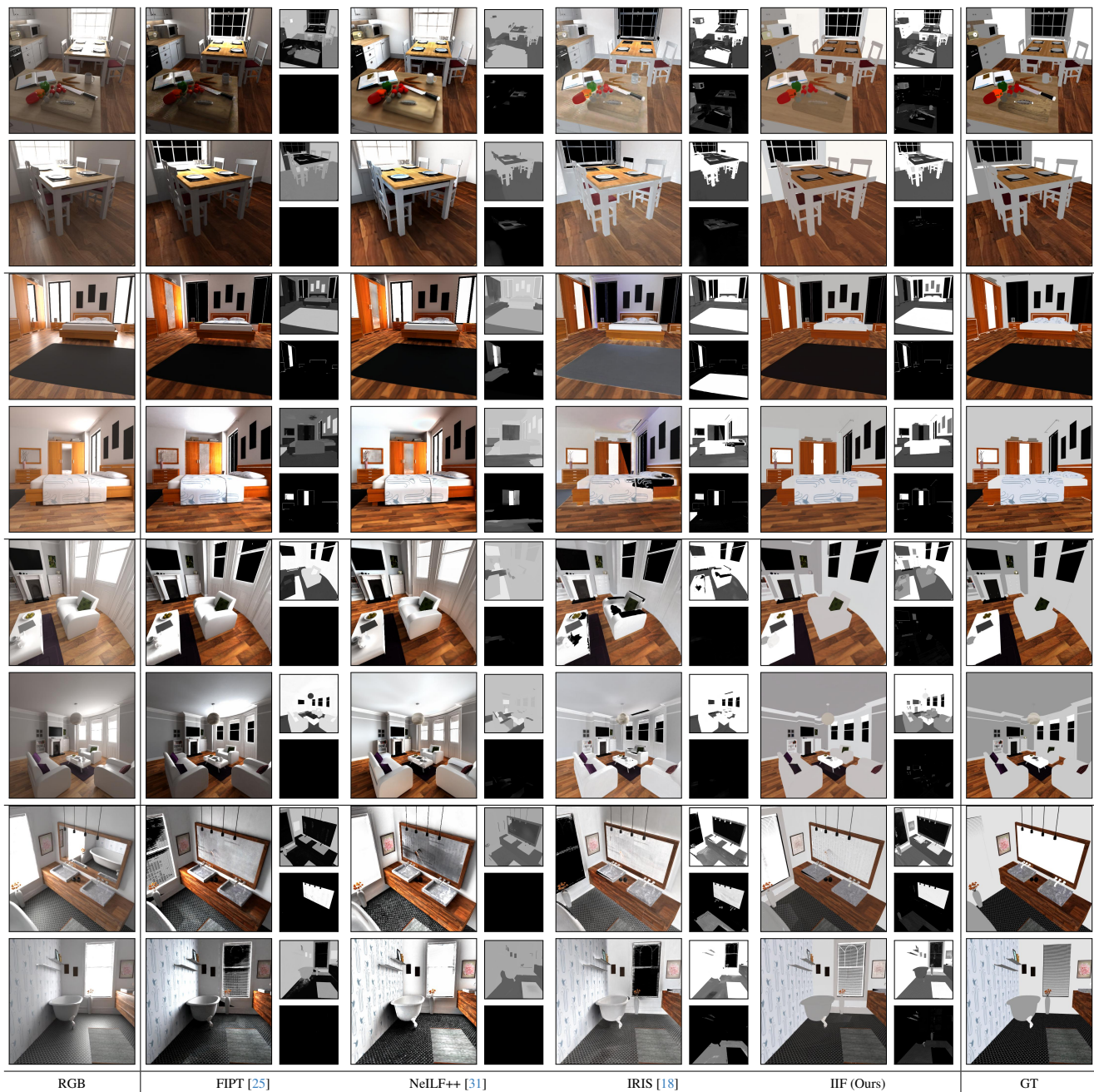


Figure 9. **Synthetic comparisons.** Additional samples on the synthetic scenes.



Figure 10. **ScanNet++ [28] comparisons.** Additional samples on ScanNet++ [28] scenes.

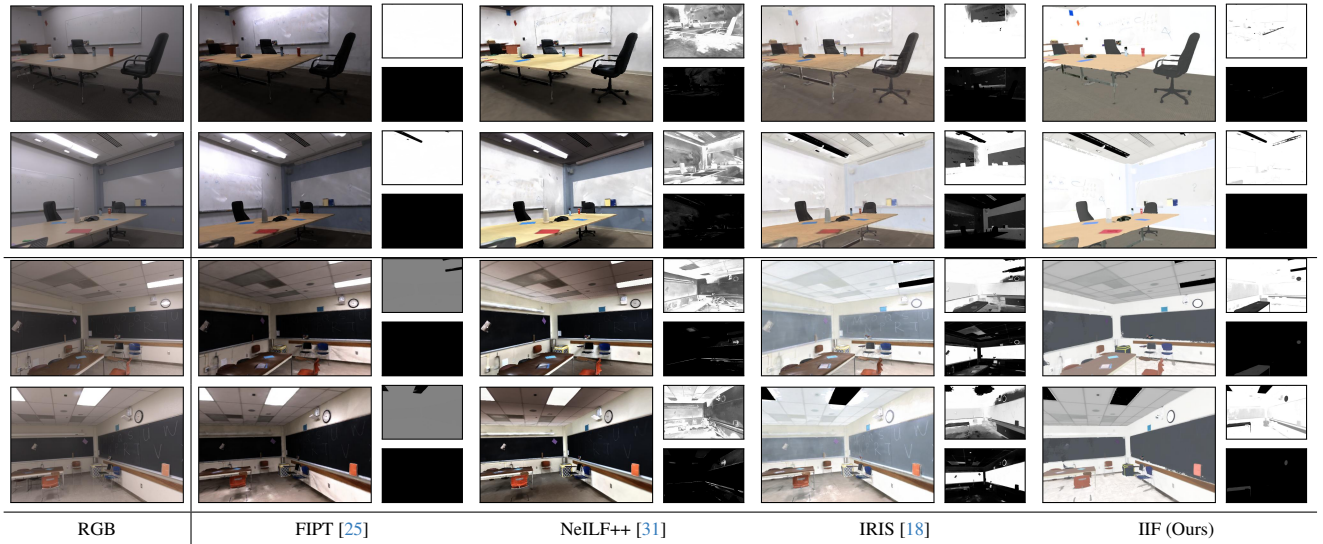


Figure 11. **Real [25] comparisons.** Additional samples on the real scenes of FIPT [25].



Figure 12. **Additional relightings.** We show additional relighting results on synthetic and ScanNet++ scenes over a smooth trajectory of an emissive sphere. For additional interpolations, please refer to our video.

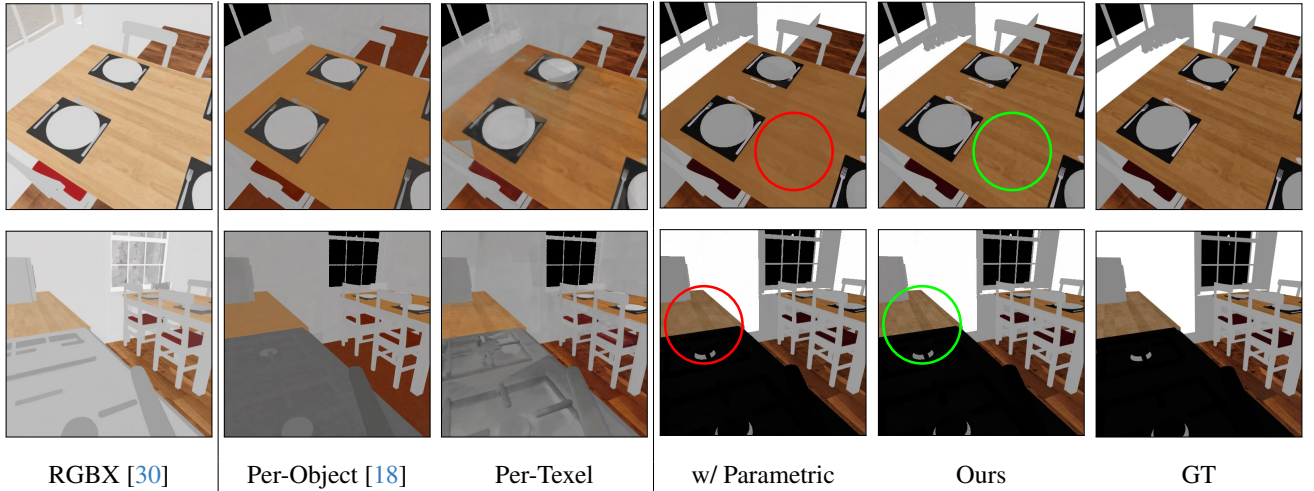


Figure 13. **Cross-view aggregation (additional results).** Single-view material estimation can yield detailed but inconsistent predictions (Fig. 2). IRIS [18] uses per-object aggregation, losing patterns. Per-texel aggregation maintains patterns but introduces seams. Our parametric modeling (§ 3.1) provides a low-dimensional space of consistent 3D aggregations. Distribution matching (§ 3.2) selects the best predictions per view to preserve fine details.